Draft version June 15, 2024
Typeset using LATEX **preprint** style in AASTeX631

History and Habitability of the LP 890-9 Planetary System

Anonymous author(s)

ABSTRACT

We present numerous aspects of the evolution of the LP 890-9 (SPECULOOS-2/TOI-4306) planetary system, focusing on the likelihood that planet c can support life. We find that the host star reaches the main sequence in 1 Gyr and that planet c lies close to the inner boundary of the **habitable zone**. We find the magma ocean stage can last up to 50 Myr, remove 8 Earth-oceans of water, and leave up to 2000 bars of oxygen in the atmosphere. However, if the planet forms with a hydrogen envelope as small as **0.1** Earth-masses, no water will be lost during the star's pre-main sequence phase from thermal escape processes. We find that the planets are unlikely to be in a 3:1 mean motion resonance and that both planets tidally circularize within 0.5 Gyr when tidal dissipation is held constant. However, if tidal dissipation is a function of mantle temperature and rheology, then we find that planet c's orbit may require more than 7 Gyr to circularize, **during which time** tidal heating may become strong enough to trigger a runaway greenhouse. We thus conclude that the habitability of planet c depends most strongly on the initial volatile content and internal properties, but no data yet preclude the viability of an active biosphere on the planet.

Keywords: astrobiology - methods: numerical - software: simulations - planets and satellites: individual: LP 890-9: dynamical evolution and stability - planets-star interactions

1. INTRODUCTION

The LP 890-9 system consists of a $0.12 M_\odot$ star and two approximately Earth-radius planets (Delrez et al. 2022), with the outer planet in or near the circumstellar habitable zone (HZ; Dole 1964; Kasting et al. 1993; Kopparapu et al. 2013). The planetary system was discovered via transits from both *TESS* and ground-based telescopes, but radial velocity data failed to achieve a detection so the masses are very poorly constrained. At a distance of 32 pc, planet c is **in** the **third** closest **system known to host at least one** potentially habitable planet **that** transits its host star, **after TRAPPIST-1 (Gillon et al. 2017) and LHS 1140 (Dittmann et al. 2017)**. At this distance, both planets' atmospheres may be amenable to follow-up spectroscopy with the *James Webb Space Telescope* (JWST) (Delrez et al. 2022). With this possibility in mind, we have performed a set of simulations that provide preliminary insight in the history and habitability of the LP 890-9 system.

We cast a wide net in our investigations, considering phenomena ranging from the geodynamo in the planetary cores to the long term evolution of the orbits. The observed and derived properties relevant to this study**, all taken from Delrez et al. (2022),** are presented in Tables 1 and 2. For

Table 1: Observed and Adopted Properties of LP 890-9

Parameter	Value	Description
L_{bol} ($10^{-3} L_\odot$)	1.44 ± 0.04	Total luminosity
T_{eff} (K)	2850 ± 75	Effective temperature
P_{rot} (d)	< 100	Rotation period
$\log(L_{H\alpha}/L_{bol})$	-4.6 ± 0.1	Normalized Hα luminosity
[Fe/H] (dex)	-0.03 ± 0.09	Metallicity
M_* ($M_\odot$)	0.118 ± 0.002	Stellar Mass
R_* ($R_\odot$)	0.1556 ± 0.0086	Stellar Radius
Age (Gyr)	$7.2^{+2.2}_{-3.1}$	Age
L_{XUV}/L_{bol}	$(5 \pm 2) \times 10^{-5}$	Adopted XUV luminosity

Table 2: Observed and Adopted Properties of the LP 890-9 Planets

Parameter	b	c	Description
m_p ($M_\oplus$)	< 13.2	< 25.3	RV upper limits
m_p ($M_\oplus$)	$2.3^{+1.7}_{-0.7}$	$2.5^{+1.8}_{-0.8}$	Adopted mass
r_p ($R_\oplus$)	$1.320^{+0.053}_{-0.027}$	$1.367^{+0.055}_{-0.039}$	Planetary radius
P_{orb} (d)	$2.7299025 \pm 3 \times 10^{-6}$	$8.4575 \pm 3 \times 10^{-4}$	Orbital period
I ($^\circ$)	$89.67^{+0.22}_{-0.33}$	$89.287^{+0.026}_{-0.047}$	Inclination w.r.t. sky plane

the non-linear and high-dimensional problem of planetary system evolution, these sets of parameters are insufficient to accurately constrain any realistic model of planet c's habitability (Meadows & Barnes 2018). We therefore augment these sets of priors with numerous other assumptions and simplifications, described and justified in §2, to predict aspects of the orbital, rotational, atmospheric, surface, and internal evolution of the star and planets.

In the next section we describe the physical models we used to simulate the system, as well as the initial conditions for our simulations. In §3, we present the results for stellar evolution (§3.1), atmospheric escape (§3.2), orbital evolution (§3.3), magma ocean phase (§3.4), and finally the post-magma ocean thermal and magnetic evolution (§3.5). We then interpret the results **in** §**4** and conclude in §5.

2. METHODS

To simulate this system, we used `VPLanet`[1], a multi-purpose planetary evolution code that breaks down the physical and chemical processes of planetary evolution into "modules" that can often be coupled together to track feedbacks (Barnes et al. 2020). In this section we first briefly review the physics employed in this study, and refer the reader to Barnes et al. (2020) and `VPLanet`'s online documentation for detailed discussions of the modules and their implementation. We then describe the details of the individual experiments we conducted.

2.1. *Physical Model*

[1] Publicly available at https://github.com/VirtualPlanetaryLaboratory/VPLanet.

The host star primarily evolves according to **a bicubic interpolation of** the Baraffe et al. (2015) model grids. These models predict (as a function of mass, age, and metallicity), the radius, bolometric (total) luminosity L_{bol}, effective temperature, and mass concentration. The XUV luminosity **follows** the Ribas et al. (2005) model, in which the initial, or "saturated," XUV luminosity (f_{sat}) remains constant for 0.1–8 Gyr, a duration called the saturation time (t_{sat}). The XUV luminosity, L_{XUV}, then decays by a power law described by a parameter we call β_{XUV} (see also Peacock et al. 2020; Johnstone et al. 2021; Richey-Yowell et al. 2022). In other words,

$$\frac{L_{\rm XUV}}{L_{\rm bol}} = \begin{cases} f_{\rm sat} & t \leq t_{\rm sat} \\ f_{\rm sat}\left(\frac{t}{t_{\rm sat}}\right)^{-\beta_{\rm XUV}} & t > t_{\rm sat}. \end{cases} \tag{1}$$

Note that the position of the HZ is only a function of L_* and T_{eff} (Kopparapu et al. 2013). LP 890-9 is a low mass star, and therefore early in its lifetime its luminosity decreased slowly over hundreds of Myr while its temperature remained approximately constant (Hayashi 1961).

In practice we begin each simulation at 5 Myr in the Baraffe et al. grids. This decision avoids any complications due to the initial physics of infall as well as instabilities in the bicubic interpolation method, which relies on numerous data points in both the time and mass dimensions. Thus, the "times" reported below are 5 Myr less than the values reported in the Baraffe et al. grids. More information about the `STELLAR` module can be found in Barnes et al. (2020), Appendix J.

The planetary orbits are influenced by both tidal interaction with the host star and the exchange of angular momentum between the planets **due to** gravitational interactions. For the long-term orbital evolution of the system, we use a constant-time-lag version of the equilibrium tide model (Darwin 1880; Goldreich & Soter 1966; Ferraz-Mello et al. 2008; Leconte et al. 2010), which reduces the tidal effects to two parameters: the tidal time lag τ (which is related to the tidal Q) and the Love number k_2. In general, tidal effects will tend to decrease the eccentricity e and semi-major axis a (Barnes 2017). The details of the `EqTide` module can be found in Barnes et al. (2020), App. E.

For the planet-planet interactions, we employ two different models depending on the goal. To examine the possibility that the planets are in a mean motion resonance (MMR), we use an N-body model, the `SpiNBody` module of `VPLanet`, that calculates the forces directly between the star and two planets. A complete description of the `SpiNBody` module can be found in Barnes et al. (2020), App. I.

The ratio of the orbital periods between planets c and b is 3.1, suggesting the planets are near, but not in, a 3:1 MMR. Recent work has shown that for first order MMRs, *e.g.,* 2:1, a separatrix exists at period ratios about 0.6% wider than perfect resonance (Goldberg & Batygin 2022), but no previous work has yet explored second order resonances. **As s**uch an analysis is beyond the scope of the current study**, w**e instead examine the likelihood of resonance the classical way: by searching for librations of the resonant arguments. For this system, three eccentricity-type resonance arguments, θ exist:

$$\theta_1 = 3\lambda_c - \lambda_b - 2\varpi_b, \tag{2}$$

$$\theta_2 = 3\lambda_c - \lambda_b - 2\varpi_c, \tag{3}$$

and

$$\theta_3 = 3\lambda_c - \lambda_b - \varpi_c - \varpi_b, \tag{4}$$

where λ is the mean longitude and ϖ is the longitude of periastron.

For long-term (Gyr) integrations, we use `VPLanet's` 4th order "secular model" (`DistOrb`) that assumes the long-term orbital evolution is well-modeled by torques between elliptical rings of matter (Ellis & Murray 2000; Deitrick et al. 2018). This method is much more computationally efficient than direct calculations, but its accuracy fades as the eccentricity and relative inclination become larger than 0.3 and 25°, respectively. The interplanetary gravitational forces will tend to drive oscillations in e and i, where i is the inclination relative to **a reference plane. In this study we set the reference plane to be** the invariable (or fundamental) plane, *i.e.,* the plane **perpendicular** to the total angular momentum vector. The `DistOrb` module is described in detail in Barnes et al. (2020), App. C.

The orbital and rotational models of the system both depend on one conservative and one dissipative model. This interplay results in many parameters evolving like damped-driven harmonic oscillators (Murray & Dermott 1999). One (or more) frequency's amplitude effectively damps to zero and the system reaches an equilibrium state. For planetary systems, the equilibrium state is typically planets with fixed non-zero eccentricities and major axes that precess in unison (Wu & Goldreich 2002).

Moving on to the planets themselves, we will consider two types of atmospheres: hydrogen-rich **worlds, which we will call** "mini-Neptunes" and hydrogen-free **worlds, which we will call "super-Earths"** (Barnes et al. 2009). For the mini-Neptune case, we assume the planet can lose hydrogen via Roche lobe overflow (Owen & Wu 2017), radiation/recombination**-limited** escape (Murray-Clay et al. 2009), or energy-limited escape (Watson et al. 1981; Erkaev et al. 2007; Luger et al. 2015). We calculate the method of loss based on instantaneous conditions, *i.e.,* as the XUV radiation evolves, the manner in which the hydrogen is lost is automatically adjusted during the integration (do Amaral et al. 2022). We employ `VPLanet`'s `AtmEsc` module to perform these calculations, which is described in Barnes et al. (2020), App. A. **Note that this model does not include any effects of molecular hydrogen on the climates of these planets (Pierrehumbert & Gaidos 2011).**

We assume super-Earths possess large initial abundances of water that erode away due to photolysis followed by H escape (Watson et al. 1981; Chassefière 1996; Luger & Barnes 2015). Our model assumes loss is initially energy-limited, but if a sufficient amount of liberated oxygen accumulates in the atmosphere, the escape becomes diffusion-limited. We assume the efficiency of the transformation of photon energy to the kinetic energy of escaping protons scales with the incident XUV flux (Bolmont et al. 2017), and is generally around 10%. **We further assume that water is only photolyzed after all of a primordial hydrogen envelope has escaped in our model and when the planet is interior to the HZ.**

Water photolysis also releases free oxygen atoms. We consider two possibilities for the fate of this liberated oxygen: 1) it accumulates in the atmosphere, where it may be dragged to space by escaping hydrogen atoms when the XUV flux is large enough (Hunten et al. 1987; Luger & Barnes 2015), or 2) it all reacts with the surface and enters the mantle. Thus, in some cases, we expect oxygen to permanently accumulate in the atmosphere.

For this study, we assume the planetary compositions are Earth-like, which may or may not be the case. We make this choice because of the relatively poor constraints on the material properties of other abundance patterns, such as larger abundances of

magnesium or calcium (see *e.g.,* Bond et al. 2010). Moreover, VPLanet's post-magma ocean interior model is only calibrated to Earth and Venus, so we limit our scope to their composition.

We **consider the possibility that** the planets form**ed** very hot with a fully molten mantle, as is likely for Earth right after the Moon-forming impact (Stevenson 1987). During this "magma ocean" phase, the volatile gases are partitioned between the interior and atmosphere in a pseudo-equilibrium (Abe 1997; Elkins-Tanton 2008; Schaefer et al. 2016) (the escaping atmosphere and secular cooling of the planet prevent actual equilibrium). Oxygen can bond with iron in the mantle to form the solid Fe_2O_3, effectively removing O from the atmosphere. As the mantle solidifies from the core/mantle boundary to the surface, water can become trapped in the mantle. To simulate the magma ocean phase, we primarily rely on `VPLanet`'s `MagmOc` module, which is described in Barth et al. (2021).

Once the mantle's melt fraction drops **to a** sufficiently low **value**, the viscosity decreases and the equilibrium between the interior and atmosphere breaks (Barth et al. 2021). This transition marks the end of the magma ocean phase and the beginning of either a plate tectonics or stagnant lid thermal/volatile/magnetic evolution (Driscoll & Bercovici 2013, 2014), which may still be affected by tidal heating (Jackson et al. 2008b,a; Henning et al. 2009; Barnes et al. 2013; Driscoll & Barnes 2015). We evaluate the post-magma ocean evolution of the planets with `VPLanet`'s `ThermInt` module, which is described in Barnes et al. (2020), App. K. **Specifically, we assume the planets evolve in a plate tectonics mode that cools the interior more rapidly than a stagnant lid planet. This choice should increase the temperature difference between the core and mantle, promoting core convection and a geodynamo.**

The above set of models provides preliminary insight into multiple aspects of the planetary system's evolution. Next we describe the parameter spaces we explored.

2.2. *Initial Conditions*

We performed 1000 simulations of the stellar evolution with each individual system's initial conditions sampled as a Gaussian according to the values in Table 1. Furthermore, **we simulated each system to a current age that is sampled from the Gaussian distribution within uncertainties listed** in Table 1. In practice, this latter choice does not affect the results. For the XUV evolution, we assumed the following initial distributions of parameters: $-3.5 \leq \log_{10} f_{sat} \leq -2.5$; 1 Gyr $\leq t_{sat} \leq$ 10 Gyr; and $-2 \leq \beta < 0$ **based on previous results for low mass M dwarfs (Peacock et al. 2020; Magaudda et al. 2020; Johnstone et al. 2021; Birky et al. 2021)**. These simulations start at **5** Myr of stellar evolution, **which planet formation models suggest is about how long it would take for these planets to fully form (Raymond et al. 2007; Lambrechts et al. 2019; Clement et al. 2022).**

We assume that the planet is fully covered by water, and some cases possess a primordial envelope made of hydrogen. We considered 3 different values of initial surface water of 1, 3, and 10 TO[2], and initial primordial hydrogen envelope **masses** of 0.001, 0.01, and 0.1 $M_\oplus$.

Moving on to the orbital evolution, we performed a suite of N-body simulations designed to evaluate the possibility that the planets are in the 3:1 resonance. Each case was integrated for 10-1000 years, or about 400-40,000 orbits of the outer planet. We found this duration was sufficient to identify librating resonant arguments. We varied both planets' mean anomaly between 0 and 360° in increments of

[2] **A "terrestrial ocean," the mass of water in modern Earth's oceans, equal to** 1.39×10^{21} **kg.**

60°; both planets' eccentricit**ies** between 0.05 and **0.3** in increments of 0.05, and the outer planet's longitude of pericenter between 0 and 360° in increments of 60°. **Note that 0.3 is the maximum eccentricity that does not cause orbit crossing at the current semi-major axes.**

To model the long-term evolution of the orbital elements, the initial eccentricities of each planet were sampled uniformly over $[0, 0.3]$. The initial longitudes of ascending node and periastron were sampled uniformly in the range $[0, 360°)$. In this parameter space, we find that the planets circularize in ∼100 Myr, see §3.3, so we don't simulate for longer timescales.

For the magma ocean phase, we explored solely the evolution of LP 890-9 c because `VPLanet`'s `MagmOc` model is currently only validated for planets in the HZ of their host star. We considered the 1σ lower and upper limit of the planet mass, respectively, and investigated initial water masses between 1 and 100 TO with 20 simulations and logarithmic scaling.

To assess the importance of long-term radiogenic and tidal heating, we ran a suite of integrations with a range of initial physical parameters. We chose planet masses within the 1σ estimate given in Delrez et al. (2022), initial eccentricities ranging between 0 and 0.5 for each planet and mantle viscosity activation energies between 2.75×10^5 and 3.5×10^5, corresponding to tidal Qs between 10 and 200. For comparison, Earth's mantle viscosity activation energy $A_\nu = 3\times10^5$. The grid spanned eight values in each dimension, for a total of 512 integrations. In all cases, we assumed Earth's **masses and abundances** of **the** radiogenic isotopes ^{40}K, ^{232}Th, ^{235}U and ^{238}U.

3. RESULTS

3.1. *Stellar Evolution*

In Fig. 1 we show the evolution of the star's bolometric luminosity, XUV luminosity, effective temperature, and radius. **While the Baraffe et al. tracks reproduce the observed luminosity quite well, they tend to be displaced by about 2 standard deviations from the best fit values of T_{eff} and radius. This results is consistent with previous analyses that found that M dwarf radii are systematically larger than theoretical predictions (*e.g.,* Morrell & Naylor 2019). However, for the purposes of our investigation, this offset is acceptable since the HZ is only weakly dependent on effective temperature, and tidal evolution of the planets will be dominated by dissipation in the planets (Mardling & Lin 2002).**

Figure 2 shows the evolution of the HZ for the range of plausible stellar masses. The limits are taken from Kopparapu et al. (2013). While planet b is always well interior to the HZ, planet c is within the "optimistic" HZ for all plausible stellar masses, and could be in the "conservative" HZ. Assuming the planets formed within several Myr (Raymond et al. 2007), planet c probably spent between 100 and 600 Myr interior to the HZ.

3.2. *Atmospheric Evolution*

Figure 3 presents the atmospheric escape results for an initial water mass of 1, 3, and 10 terrestrial ocean (TO) in a range of initial hydrogen envelope masses. The results show that both planets can lose up to 9.9 TO in the first 370 Myr if they did not possess a primordial hydrogen envelope. In these scenarios, when the initial amount of water is 10 TO, the oxygen in the atmosphere reaches up to 1900 bars. In the early stage of evolution, during the first 1 Gyr, a small hydrogen envelope of 0.01 - 0.1 $M_\oplus$ is sufficient to prevent water escape.

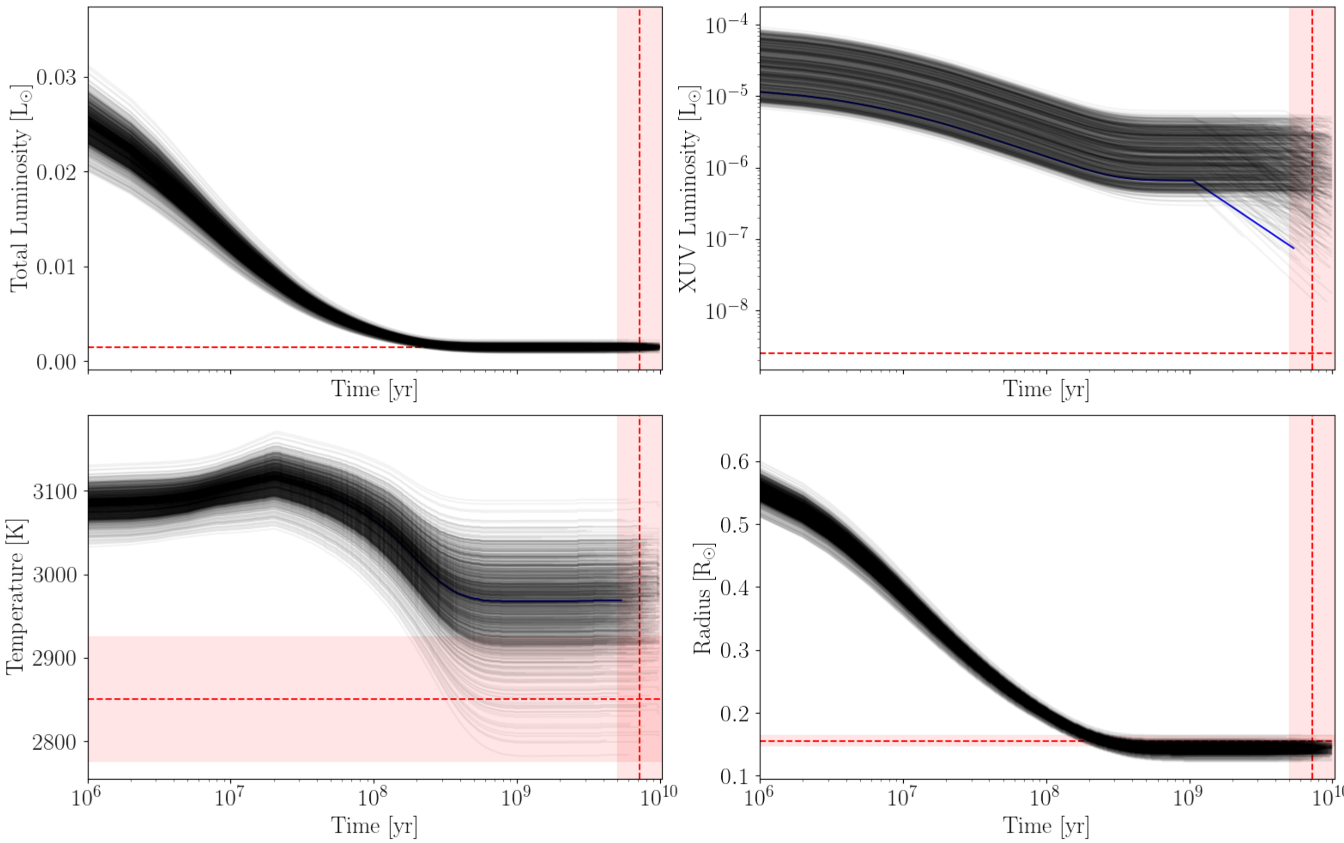

Figure 1. Revised figure. Evolution of some of LP 890-9's stellar properties. **Note that the "Time" in each panel is offset by 5 Myr from the Baraffe et al. (2015) model grids that form the foundation for the stellar evolution model, see §2.1.** Each panel includes 10% of 1000 trials sampled within the ranges described in the text. The red lines and shading represent the best fit and 1-σ uncertainties of each parameter, if available. *Top left:* Total bolometric luminosity. *Top right:* XUV luminosity. The blue curve is the **best fit** history of the star. *Bottom left:* Effective temperature. *Bottom right:* Radius.

Another feature that helps keep the water on the surface is the presence of oxygen in the atmosphere. Since oxygen can be dragged into space by the hydrogen, less energy is available for photolysis and the kinetic energy of the hydrogen atoms. **If we compare all the panels in the first row from Figure 3, we can notice that for the same age, the planets lose more water if the oxygen is absorbed by the surface, compared to when the oxygen remains in the atmosphere.**

These figures reveal that envelopes masses of $0.1M_\oplus$ and larger cannot be fully stripped during the pre-main sequence phase of the host star. These envelopes inflate the radius of the planet beyond the observed value and are therefore disfavored. However, after 7.5 Gyr of evolution, the results shown in left panel of Figure 4 indicate that these planets could have started with a H/He inventory in between 0.01-0.1 $M_\oplus$.

The results also show that the incoming XUV flux is initially hundreds of W/m^2, but drops quickly **(bottom panel of Figure 4). Due to this high XUV flux, the crossover mass at the beginning of the evolution is larger than 16 amu (fourth panel of Figure 3), which means that the hydrogen can drag the oxygen to space. But as the XUV flux drops, the crossover mass drops below 16 amu and there is no longer a flux of O atoms to space.**

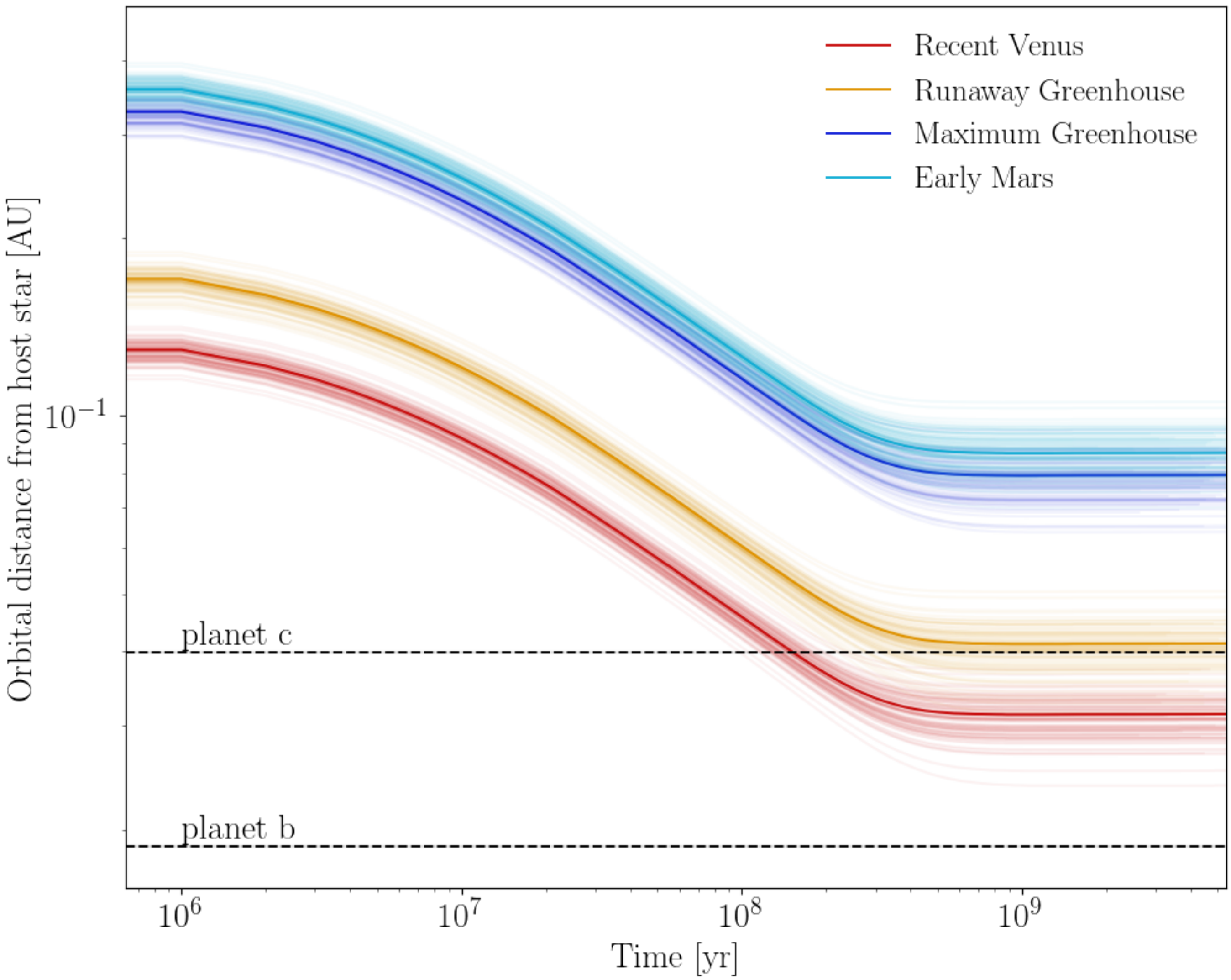

Figure 2. Evolution of LP 890-9's HZ for 10% of the 1000 trials. The pale blue curves correspond to the "early Mars" limit, dark blue to "maximum greenhouse," orange to "runaway greenhouse" and red to "recent Venus" (Kopparapu et al. 2013). Thin curves represent individual trials, while the thick line is the average. The current orbits of planets b and c, assuming the best fit stellar mass, are shown with dashed black lines.

The panels of the second row show the amount of oxygen that is absorbed by the surface. Planet b loses up to 67 bars and planet c loses up to 41 bars of oxygen to space when the planets begin with an initial surface water content of 10 TO. However, not all scenarios present extreme scenarios, such as total desiccation. **Simulations with an initial hydrogen envelope mass of $> 0.01\mathrm{M}_\oplus$ can keep all the surface water, regardless of the initial amount of water on the surface.**

3.3. *Orbital Evolution*

Next we turn to the orbital evolution of the system. We begin by examining the likelihood that the planets are in a 3:1 mean motion resonance. Of our 13,824 simulations, we found only 6 cases **for** which the resonance arguments librated, see Eqs. (2)–(4). Even then, the amplitudes were nearly 360°, suggesting that the resonant effects are still very weak. We therefore conclude that we can

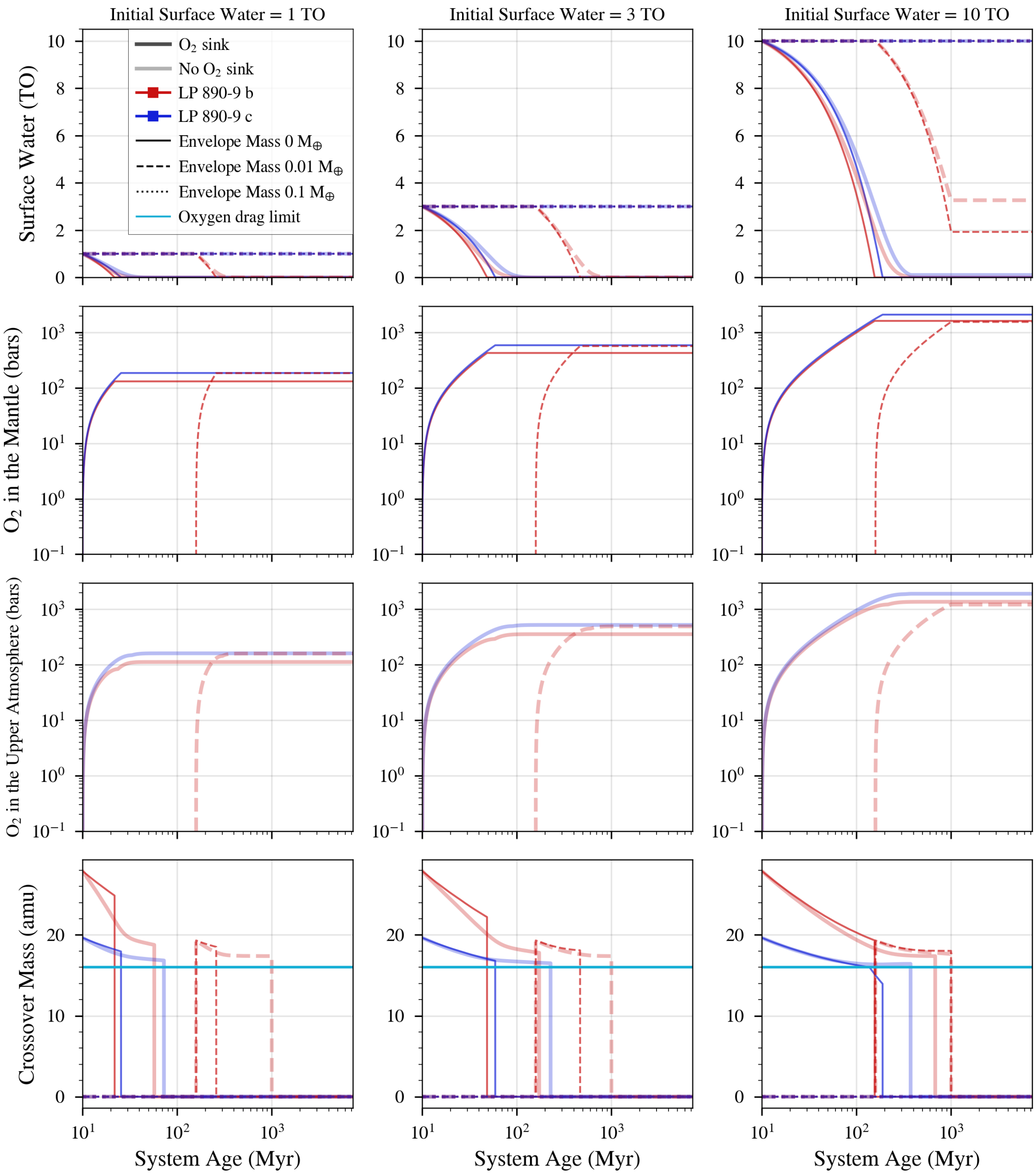

Figure 3. Revised Figure. Evolution of the atmospheric parameters for LP 890-9 b (red) and c (blue), with an initial surface water content of 1 TO (left panels), 3 TO (middle panels), and 10 TO (right panels). *First row:* **Surface water content. The solid, dashed, and dotted curves represent an initial envelope mass of 0, 0.01, and 0.1 $M_\oplus$, respectively. Curves with high and low opacity represent the cases when the oxygen does or does not react with the surface, respectively.** *Second row:* **O_2 sink in the mantle.** *Third row:* **O_2 accumulated in the atmosphere** *Fourth row:* **Crossover mass. The horizontal light blue line represents the limit where the oxygen can be dragged along the hydrogen background out of the atmosphere.**

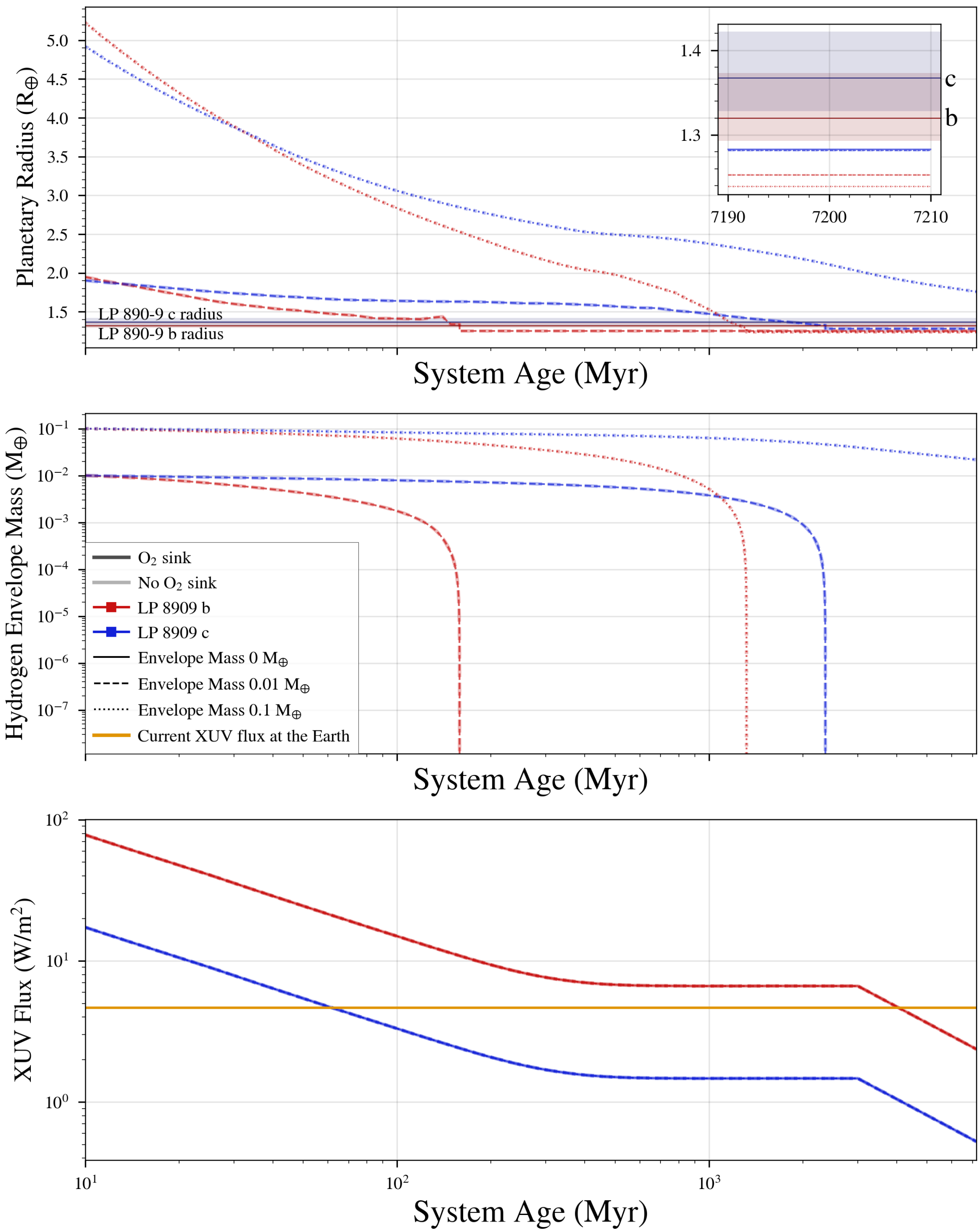

Figure 4. New Figure. Time evolution of planetary radius (upper panel), hydrogen envelope mass (middle panel), and XUV flux at the planetary atmosphere (bottom panel). The horizontal orange line in the bottom panel indicates the XUV flux on the present Earth. Horizontal lines in the top panel indicate the observed planetary radii of LP 890-9 b and c (Delrez et al. 2022). The shadow in the inset of the top panel shows the planetary radius uncertainty.

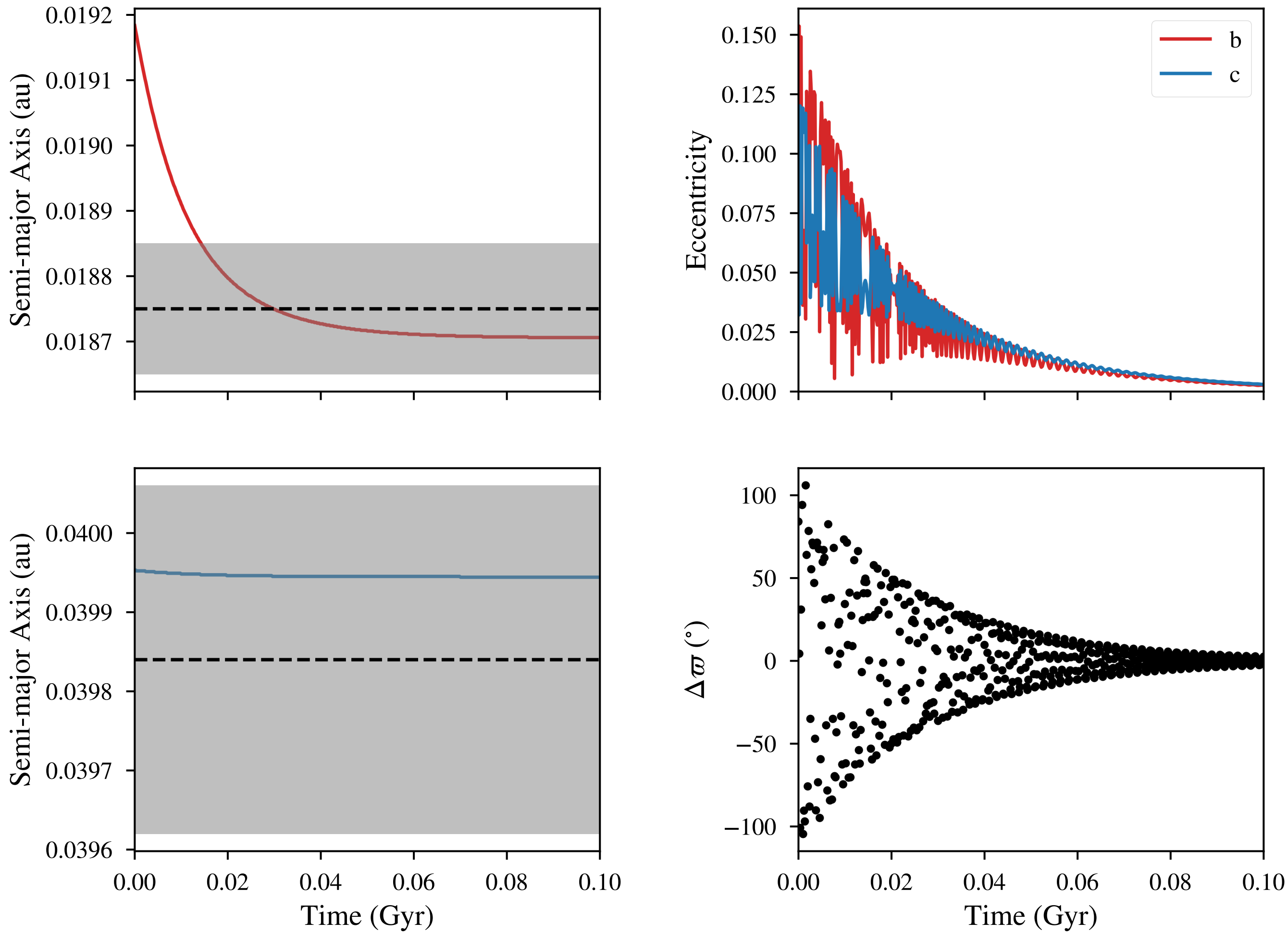

Figure 5. Example of the coupled tidal + orbital evolution of the LP 890-9 planetary system over 100 Myr. Dashed lines represent the best fit values and the shaded grey regions demarcate the 1σ credible intervals from Delrez et al. (2022).

safely ignore the 3:1 MMR and simulate the system with a secular orbital evolution model.

Figure 5 shows an example of the **tidal-**secular orbital evolution of the system, specifically the semi-major axes a, eccentricities e, and the difference between their longitudes of periastron $\Delta\varpi$. This simulation reproduces the observed semi-major axes within observational uncertainties (Delrez et al. 2022) after 100 Myr, but is very likely not the true trajectory because the magnitude and frequency dependence of the tidal dissipation model are poorly approximated by equilibrium tide theory (see e.g., Touma & Wisdom 1993; Efroimsky & Makarov 2013; Greenberg 2009).

Tidal effects drive both eccentricities to < 0.01 after ~ 100 Myr, while the perturbations between the planets drive sinusoidal oscillations. The result is effectively a damped-driven harmonic oscillator that ultimately **circularizes** both planets' orbits. Once the orbits have circularized, the tidal evolution of the semi-major axes can only proceed via dissipation in the star (Mardling & Lin 2002; Raymond et al. 2008).

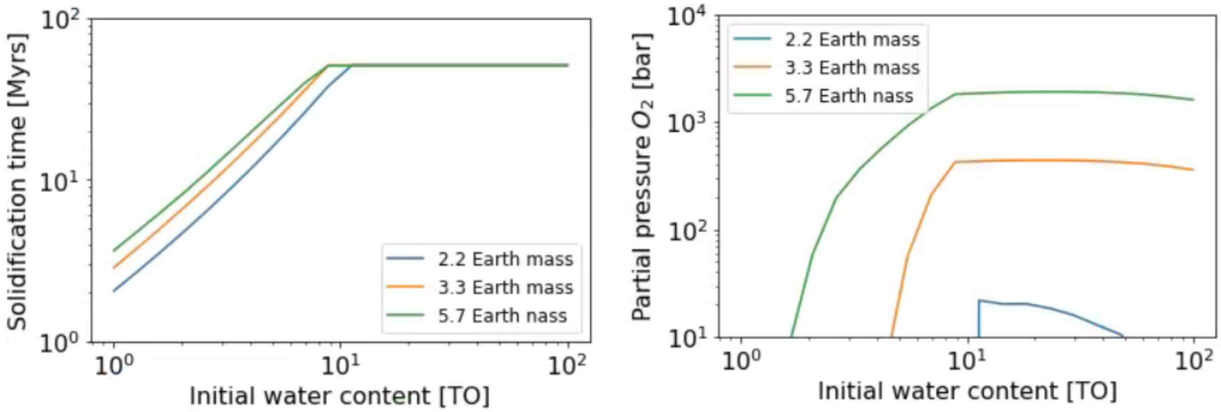

Figure 6. *Left:* Magma ocean solidification time of LP 890-9 c versus initial water content in TO for different planetary masses. Solidification times below 51 Myrs require less than ~10 TO of primordial water. *Right:* Abiotic oxygen build-up (partial pressures of O_2 in bar) in LP 890-9 c during the magma ocean stage as a function of initial water mass.

3.4. *Magma Ocean Evolution*

We find **that** the duration of the magma ocean phase depends on the initial water content and can be up to 51 Myr, as shown in Fig. 6. For 1 TO the magma ocean can solidify in just a few hundred thousand years, depending on the planet's mass. In these respects, the simulated LP 890-9 c magma ocean evolution resembles that of TRAPPIST-1 e as outlined in Barth et al. (2021), which **is also close to** the inner edge of the habitable zone of its host star.

Water loss leads to the abiotic build-up of oxygen in the atmosphere once the iron buffer in the mantle has be**en** fully **exhausted**. We find that the oxygen surface pressures can range from 400 bars ($3.3 M_{Earth}$) **to** 2000 bars for ($5.7 M_{Earth}$). For the lowest planetary mass, $2.2 M_{Earth}$, oxygen build-up is suppressed as we find that the majority of the oxygen produced by photolysis of H_2O is lost to space. Figure 7 shows the abundances of water and oxygen in the various reservoirs over time for an initial water mass of 5 TO.

3.5. *Thermal and Magnetic Evolution*

A fiducial case of the thermal and magnetic evolution of planets b and c is shown in Figure 8. While the exact parameters at 7.2 Gyr will change depending on the initial parameters in mass, eccentricity, and mantle viscosity activation energy, the general evolution will be similar to **that** shown in Figure 8. From this fiducial run, we can see that, despite having similar planetary masses, the differing levels of tidal heating between the two planets result in significant differences in their thermal evolution.

For LP 890-9 b, the orbit circularizes quickly (bottom left panel), resulting in **almost** no contribution to the internal heat budget from tidal heating (top right panel). In contrast, LP 890-9 c **experiences tidal heating that reaches 1 TW at 0.1 Gyr, and 1000 TW at 10 Gyr (Earth's internal power is 40 TW). The impact of this powerful heating is, however, modest in terms of internal temperatures. In the top middle panel, we see the mantle temperatures begin to diverge at** ~ 0.05 **Gyr, reaching a maximum difference between the two planets of about 75 K at** ~ 2 **Gyr.**

This relatively small difference in mantle temperature creates a qualitative difference in the core temperature evolutions. In the top left panel we see that up to 0.05 Gyr,

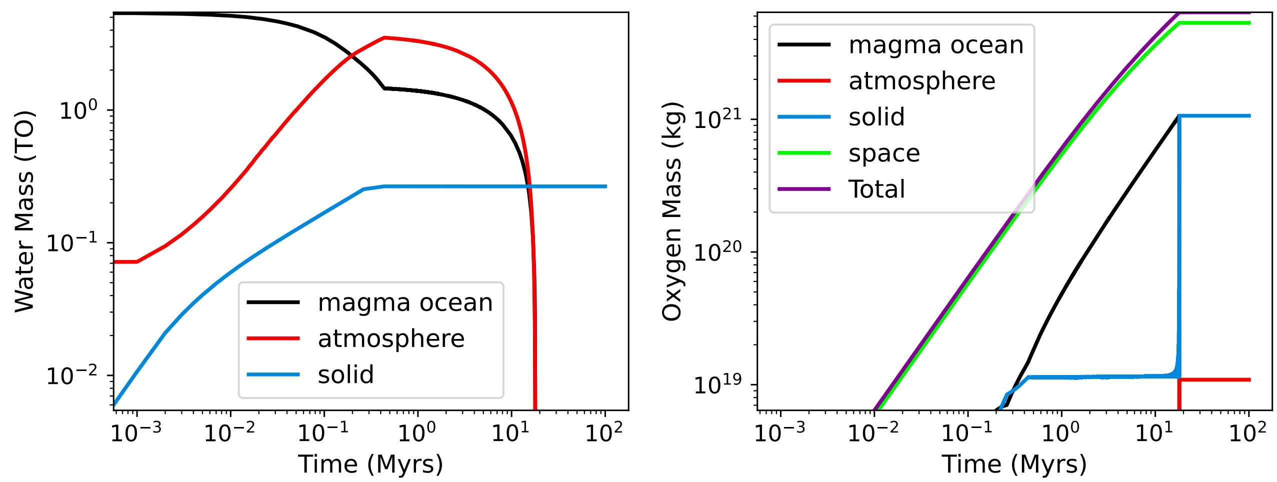

Figure 7. Example simulation of LP 890-9 c assuming a mass of 2.2 $M_\oplus$ and 5 TO of initial water content. *Left:* Water evolution during the magma ocean stage shows **all water is lost from the atmosphere after** 18 Myr. *Right:* Oxygen evolution during the magma ocean stage, where the majority of the O_2 escapes into space.

the core temperatures are nearly equal and constant, but that afterwards b's core temperature decreases while c's increases by about 30 K before rapidly falling off at about 1 Gyr. This divergence is due to the competing effects of a hotter mantle and radiogenic heating from potassium (half-life = 1.8 Gyr) in the core. Initially the cores are in thermodynamic equilibrium with the mantles as core cooling into the mantle is approximately offset by radiogenic heating. As planet c's mantle temperature increases due to tidal heating, the temperature difference decreases, resulting in slower core cooling. Thus, the core heats up by about 30 K. After 1-2 Gyr, potassium heating fades and the mantles continue to cool, both of which increase core cooling and instigate the steeper temperature drop in planet c's core seen in the top left panel of Fig. 8.

The different core and mantle thermal evolutions is also reflected in the magnetic field strengths. With a shallower temperature gradient between planet c's core and mantle, we would expect its liquid core to experience less vigorous convection and hence generate a weaker dynamo. The bottom middle panel confirms this expectation as planet c's dynamo appears to be about 10x weaker throughout much of its history. In `VPLanet`'s 1D model, the dynamo is independent of $\dot{T}_c$, so the brief period in which the core warms does not affect dynamo generation. The discontinuity both magnetic moments show at later times is due to inner core nucleation, which provides additional core heating in the from of latent heat.

Although this thermal evolutionary model does not strictly include a magma ocean phase, the effects of a high mantle temperature are visible in Figure 8. As the temperature drops, the melt fraction also drops and after 1 Myr the mantle viscosity increases dramatically as a result. Convection in the stiffer mantle slows cooling, and as a result the mantle temperature becomes approximately constant. We emphasize, though, that

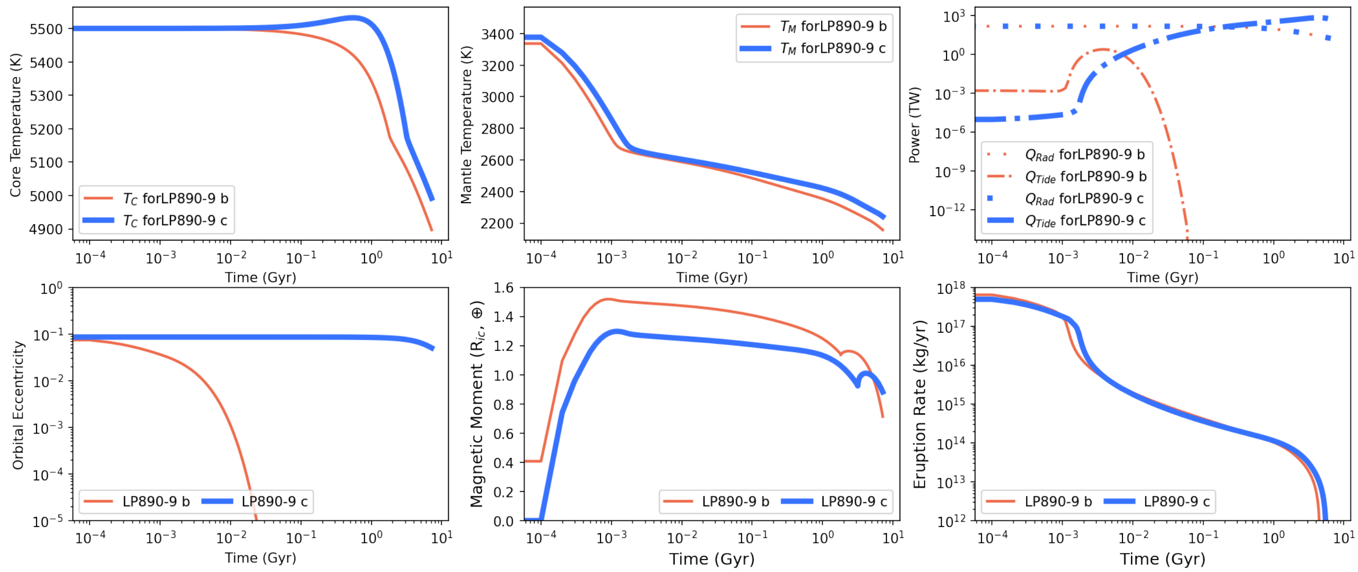

Figure 8. An example of the thermal and magnetic evolution of LP 890-9 b and c from the `EqTide`, `ThermInt`, and `RadHeat` modules. Both fiducial integrations are representative cases from the larger integration set presented in Figure 9, with the viscosity activation energies of $A_{v,b} = 2.9 \cdot 10^5$ and $A_{v,c} = 3.1 \cdot 10^5$ chosen so that both planets have approximately equal initial tidal $Q \approx 30$. Both planets have initial eccentricities of $e \sim 0.1$, and masses of $m_b = 2.3M_\oplus$ and $m_c = 2.9M_\oplus$. The interior structures of both planets are otherwise assumed to be Earth-like. Throughout the integration, LP 890-9 c has a consistently higher core temperature and generally has a higher mantle temperature than LP 890-9 b. In the upper right panel, we see that LP 890-9 b's internal heat budget is driven by radiogenic heating for the full integration lifetime, while LP 890-9 c has a significant contribution from tidal heating, which increases in total power as its orbital eccentricity begins to decay by the end of the integration (bottom left panel). Both planets have non-zero magnetic moments for the majority of the integration, and experience declining eruption rates as the planets age.

these simulations did not include the full geochemical evolution of the magma ocean, and so evolution during the first million years should be ignored.

The top right panel of Figure 8 shows the relative importance of two major internal heat sources: radiogenic heating and tidal heating. Radiogenic heating is supplied by radioactive isotopes present in the planetary interior, and the rate of heating depends only on the abundance of those isotopes. In contrast, tidal heating occurs due to tidal strain dissipated in the planetary interior, and is a function of e and rotation period. For the fiducial case given in Figure 8, the orbit of the inner planet LP 890-9 b circularizes well before the present day, resulting in the internal heat budget being fully provided by radiogenic heating. In contrast, the outer planet LP 890-9 c still maintains significant planetary eccentricity by a stellar age of 7.2 Gyr, meaning that the internal heat budget comes from multiple sources.

We ran integrations of the system's interior evolution over these bounds, and in Figure 9 we plot the ratio of the radiogenic heating to the total heating (when the total includes contributions from radiogenic and tidal heating). The two planets have different bounds of potential evolution: LP 890-9 b shows evidence of some contribution from tidal heating at early times, but by 7.2 Gyr all system realizations approach a ratio of 1; in contrast, LP 890-9 c allows any value of the ratio, with the most likely value at 7.2 Gyr being 0. From these parameter sweeps, we can conclude that LP 890-9 b's internal heat budget is supplied solely by radiogenic heating today. In contrast, while LP 890-9

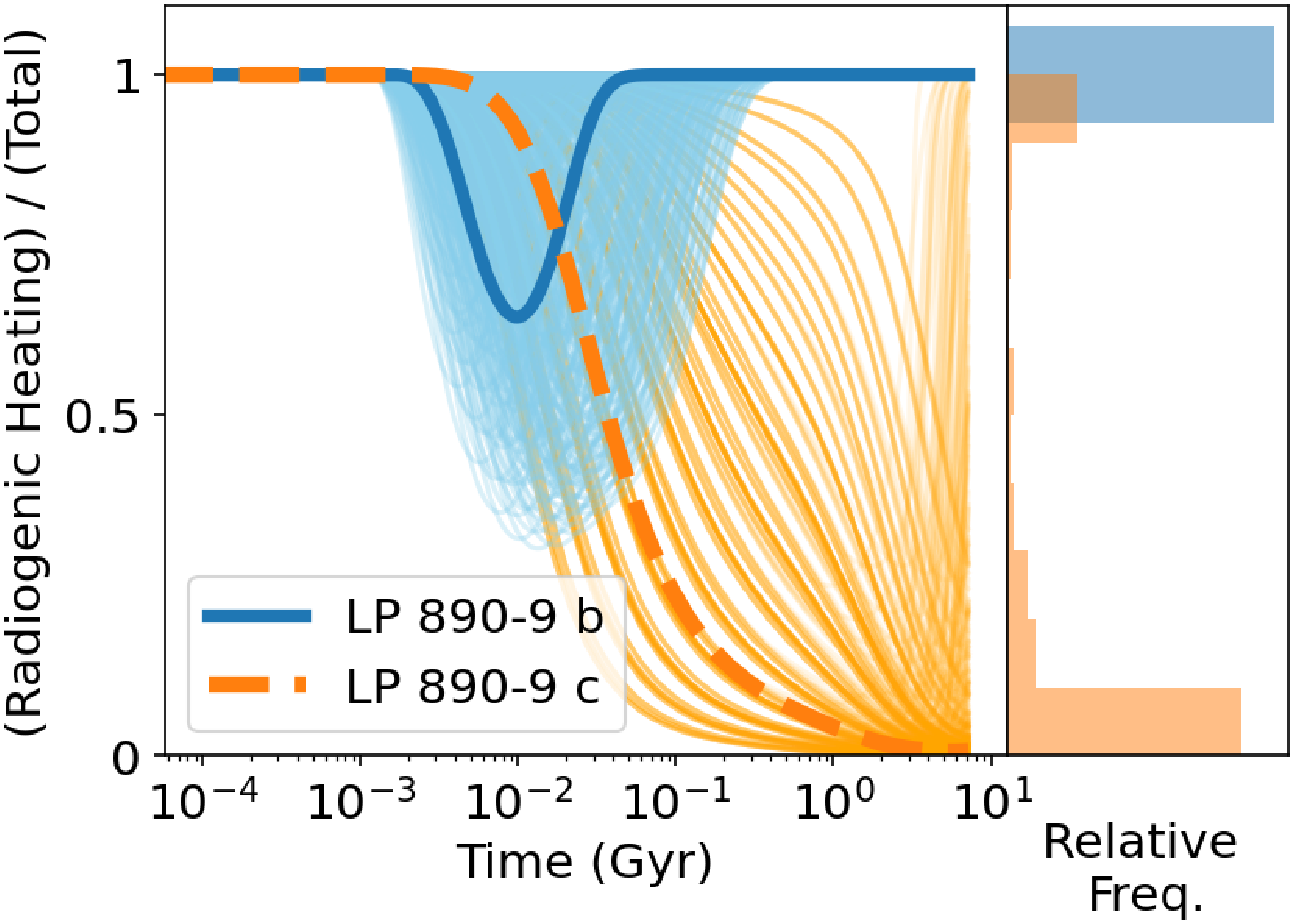

Figure 9. The results of a parameter sweep over the mass, orbital eccentricity, and viscosity activation energy for each planet. Individual trials are plotted as thin solid curves. The evolution of the fiducial case is overlaid in the left panel with thick curves. The distribution of the fraction of the total internal heat generated by radiogenic heating at **the** present day (a stellar age of 7.2 Gyr) is plotted as a histogram for each planet in the right panel. The orbit of the inner planet, LP 890-9 b, always circularizes by the end of the integration, leaving the primary source of internal heating to be radiogenic heating in all integrations. The outer planet, LP 890-9 c, has a much more varied range of heating ratios at the end of the integration, so that the primary internal heat source at present day cannot be securely determined.

c's heat budget might be supplied by solely radiogenic heating, predominantly tidal heating, or by a combination of the two in a variety of ratios.

To assess how the planetary mass and eccentricity of LP 890-9 c affects its total tidal power, we used an additional parameter sweep over these two variables. We expanded the range of parameters under consideration compared to the previous case, considering masses within the 2σ mass limits from Delrez et al. (2022) and eccentricities up to 0.5 (note that for $e_b = 0$, this value would be the limit above which orbits would cross). The results are shown in Figure 10. We see that for combinations of larger e_c and lower m_c, the orbits have circularized and there is no tidal power left at 7.2 Gyr. This section of the phase space corresponds to the integrations in Figure 9 that show the interior heat coming only from radiogenic heating. For larger masses and larger eccentricity

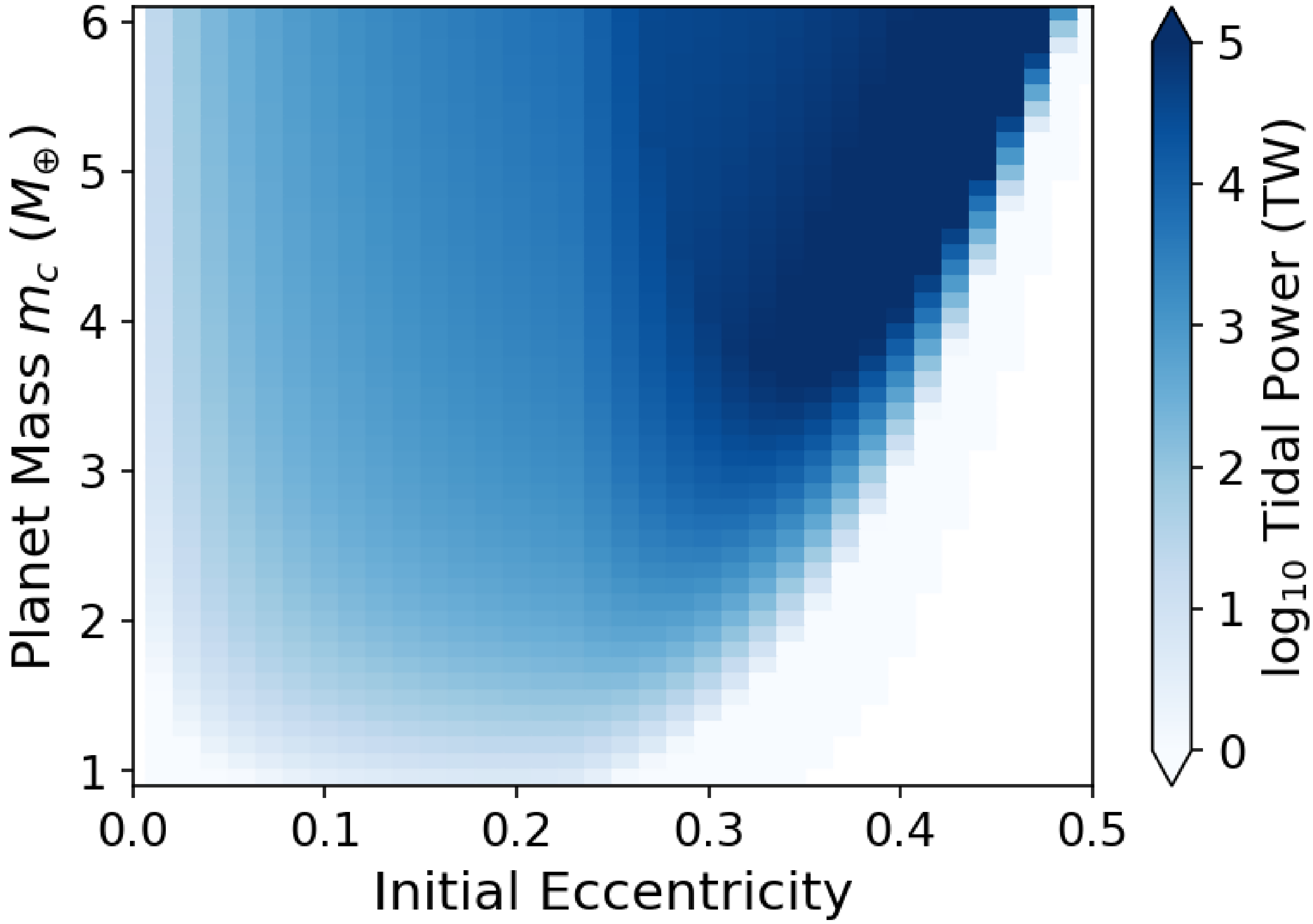

Figure 10. A parameter sweep computing the tidal power after 7.2 Gyr for a range of eccentricity (sampled between 0 and 0.5) and mass of LP 890-9 c (sampled over the 2σ error bounds, 0.9 - 6.1 $M_\oplus$) for an interior structure corresponding to an initial tidal $Q = 17$ **(commensurate with values for the terrestrial planets given in Goldreich & Soter 1966)**. The white region of the plot indicates no tidal power after 7.2 Gyr, which occurs because the planetary orbit has circularized. For larger planetary eccentricities and masses, the tidal power after 7.2 Gyr remains substantial and would provide significant surface heating. An analogous plot for LP 890-9 b is not presented because all tested orbits circularized by the end of the integrations resulting in no tidal power.

values ($m_c > 3M_\odot; e_c > 0.25$), the tidal power after 7.2 Gyr is significant, reaching values upwards of $10^4 - 10^5$ TW. For comparison, Io's total tidal power is roughly 100 TW (Veeder et al. 1994), a value which drives total mantle melt and results in runaway mantle melt and extreme surface volcanism (Peale et al. 1979). For values of $e_c < 0.2$, the tidal power is closer to $10^1 - 10^2$ TW at present day.

4. DISCUSSION

The results presented here reveal numerous possibilities for the evolution of the LP 890-9 system and the potential habitability of planet c. Crucially, we find no reason to conclude at this time that LP 890-9 c cannot support life. Of course, there are many reasons to still be cautious about that possibility, and the research presented herein illuminates many of those reasons, as well as valuable directions of future research that could resolve the ambiguities.

Starting with the star, the lack of knowledge of the current XUV luminosity is a major missing piece for assessing habitability. As the incident XUV flux is a primary driver of water destruction (Watson et al. 1981; Erkaev et al. 2007; Luger & Barnes 2015), observations of this parameter are probably the most important for assessing habitability. The XUV evolution could potentially be further constrained if the stellar rotation rate were measured, which can provide constraints on the stellar convective Rossby number, which is tightly correlated with activity and high energy radiation (*e.g.,* Barnes 2003; Garraffo et al. 2018; Johnstone et al. 2021). Combining a model of stellar rotation evolution with the observed XUV luminosity could provide much stronger constraints on the XUV saturation time and fraction, as well as the subsequent XUV luminosity decay.

Moving onto the planet itself, the biggest missing piece is the planetary mass. Without the mass, we cannot estimate the gravitational acceleration at the surface, which is a key controller of atmospheric escape. If future radial velocity or transit timing variations (Agol et al. 2005; Holman & Murray 2005) could weigh the planets and add that constraint to the models presented here, then they would be significantly more accurate.

Measuring the planetary mass could also **provide** clues to planetary composition. Here we have assumed an Earth-like composition, which influences processes such as internal temperature, viscosity, magnetic field strength, and tidal effects. While a comprehensive understanding of how composition affects the full range of planetary processes is not yet available, knowledge of the composition could nonetheless help constrain the thermal and volatile evolution of the planets.

We find that planet c could lose 10 TO of water due to thermal escape, consistent with other results for planets orbiting low mass stars (Luger & Barnes 2015; Bolmont et al. 2017; do Amaral et al. 2022). The water loss process could result in hundreds of bars of oxygen in the atmosphere or chemically absorbed by the surface. Alternatively, just 0.001$M_\oplus$ of primordial hydrogen could protect the planet's water and allow the planet to emerge as a "habitable evaporated core" after the hydrogen envelope is completely lost (Luger et al. 2015; do Amaral et al. 2022). We caution, however, that our models are relatively simple and future work could use more sophisticated models to further refine water loss predictions (Cohen et al. 2015; Brain et al. 2016; Dong et al. 2018; Airapetian et al. 2020).

We find the orbital evolution is probably not a major influence on the potential habitability of planet c. Although we could not determine if the planets are in a 3:1 MMR, its effects are likely to be weak because the period ratio is significantly different from the exact commensurability. The long-term tidal/orbital evolution is not likely to result in significant semi-major axis evolution, at least for initial eccentricities below 0.2. **Previous work has shown that** the planetary spins are likely to synchronize within a few tens of kyr (Barnes 2017), and the obliquities damp to equilibrium values that are well below 1° (Dobrovolskis 2009; Heller et al. 2011), and hence the planets are likely only illuminated on one hemisphere.

The long-term geophysical evolution of planet c, however, could preclude habitability for certain cases with large initial eccentricity. In the Maxwell rheology employed here, planet c could experience a large burst of tidal heating after Gyr of evolution, especially if the planet is relatively massive. In those cases, the tidal heat flux at the surface could approach or exceed the runaway greenhouse limit (Barnes et al. 2013; Driscoll & Barnes 2015). Thus, the planet could be habitable for several Gyr, only for the mantle temperature to reach the "Maxwell peak" that generates a large enough heat flux to sustain a desiccating runaway greenhouse. It remains unclear how realistic this rheological model is, but, **if real**, it is clearly a threat to planetary habitability.

5. CONCLUSIONS

The LP 890-9 system offers an enticing opportunity to study planetary evolution and habitability around low mass stars. The presence of an Earth-sized planet in the HZ is sufficient to warrant further scrutiny, and our analysis has provided more reasons to turn large space-borne telescopes toward this system. Regardless of habitability, the planetary atmospheres could provide clues to the atmospheric, internal, and orbital evolution of any terrestrial planet orbiting a low-mass star.

The most serious threats to habitability are a persistent or transient runaway greenhouse, which ultimately results in the destruction of water. The early pre-main sequence brightness of the star could desiccate planet c before it ever reaches the habitable zone (Luger & Barnes 2015), or a more recent "tidal greenhouse" (Barnes et al. 2013; Driscoll & Barnes 2015) could permanently destroy habitability at later times. While these threats are real, our analysis cannot confirm that they occurred, hence the ability of LP 890-9 c to support life remains an open question. **However, the LP 890-9 system adds to the limited sample of objects available for investigating demographic imprints of the inner boundary of the HZ (Turbet et al. 2019; Schlecker et al. 2024).**

Our investigation has confirmed that future research should focus on measuring the current XUV luminosity of the star and the planetary masses. X-**r**ay and UV measurements could be made that are similar to TRAPPIST-1 (Becker et al. 2020), while transit timing variations could reveal their masses (see, *e.g.,* Agol et al. 2021). Furthermore, if the composition of the star could be measured and/or the **processes that formed these** worlds be determined, then the composition of the planets could be constrained (Bond et al. 2010).

Future research should also improve upon the modeling efforts described above. While our study has examined many aspects of planetary evolution, it is still deficient in many areas. In particular, the role of carbon dioxide in the interior and atmosphere must be addressed (see *e.g.,* Krissansen-Totton & Fortney 2022). As CO_2 is a heavy molecule and a powerful greenhouse gas, it could accumulate in the atmosphere for Gyr and help heat the surface into a runaway greenhouse. Ultimately, a model that **connects** the magma ocean, stagnant lid/plate tectonics geochemistry to orbital evolution and improved XUV histories will provide **better** insight into planet c's habitability prior to direct atmospheric characterization. `VPLanet` possesses many of the pieces of such a model, but significant effort will be required to properly couple and validate the physics and chemistry.

As one of just a few potentially habitable planets that transits stars in the solar neighborhood, LP 890-9 c is a very valuable target in the search for life beyond the Solar System. While our research cannot provide many definitive statements about the history and habitability of the LP 890-9 system, it has revealed numerous intriguing possibilities and clarified directions of future research. Our investigations provide a starting point for further characterizing this system, and perhaps the first discovery of active biology on an exoplanet.

REFERENCES

Abe, Y. 1997, Physics of the Earth and Planetary Interiors, 100, 27, doi: 10.1016/S0031-9201(96)03229-3

Agol, E., Steffen, J., Sari, R., & Clarkson, W. 2005, *Mon. Not. R. Astron. Soc.*, 359, 567, doi: 10.1111/j.1365-2966.2005.08922.x

Agol, E., Dorn, C., Grimm, S. L., et al. 2021, *Plan. Sci. J.*, 2, 1, doi: 10.3847/PSJ/abd022

Airapetian, V. S., Barnes, R., Cohen, O., et al. 2020, International Journal of Astrobiology, 19, 136, doi: 10.1017/S1473550419000132

Baraffe, I., Homeier, D., Allard, F., & Chabrier, G. 2015, *Astron. & Astrophys.*, 577, A42, doi: 10.1051/0004-6361/201425481

Barnes, R. 2017, Celestial Mechanics and Dynamical Astronomy, 129, 509, doi: 10.1007/s10569-017-9783-7

Barnes, R., Jackson, B., Raymond, S. N., West, A. A., & Greenberg, R. 2009, *Astrophys. J.*, 695, 1006, doi: 10.1088/0004-637X/695/2/1006

Barnes, R., Mullins, K., Goldblatt, C., et al. 2013, Astrobiology, 13, 225, doi: 10.1089/ast.2012.0851

Barnes, R., Luger, R., Deitrick, R., et al. 2020, Publications of the Astronomical Society of the Pacific, 132, 024502, doi: 10.1088/1538-3873/ab3ce8

Barnes, S. A. 2003, *Astrophys. J.*, 586, 464, doi: 10.1086/367639

Barth, P., Carone, L., Barnes, R., et al. 2021, Astrobiology, 21, 1325, doi: 10.1089/ast.2020.2277

Becker, J., Gallo, E., Hodges-Kluck, E., Adams, F. C., & Barnes, R. 2020, *Astron. J.*, 159, 275, doi: 10.3847/1538-3881/ab8fb0

Birky, J., Barnes, R., & Fleming, D. P. 2021, Research Notes of the American Astronomical Society, 5, 122, doi: 10.3847/2515-5172/ac034c

Bolmont, E., Selsis, F., Owen, J. E., et al. 2017, *Mon. Not. R. Astron. Soc.*, 464, 3728, doi: 10.1093/mnras/stw2578

Bond, J. C., O'Brien, D. P., & Lauretta, D. S. 2010, Astrophys. J., 715, 1050. https://arxiv.org/abs/1004.0971

Brain, D. A., Bagenal, F., Ma, Y. J., Nilsson, H., & Stenberg Wieser, G. 2016, Journal of Geophysical Research (Planets), 121, 2364, doi: 10.1002/2016JE005162

Chassefière, E. 1996, J. Geophys. Res., 101, 26039, doi: 10.1029/96JE01951

Clement, M. S., Quintana, E. V., & Quarles, B. L. 2022, *Astrophys. J.*, 928, 91, doi: 10.3847/1538-4357/ac549e

Cohen, O., Ma, Y., Drake, J. J., et al. 2015, *Astrophys. J.*, 806, 41, doi: 10.1088/0004-637X/806/1/41

Darwin, G. H. 1880, Royal Society of London Philosophical Transactions Series I, 171, 713

Deitrick, R., Barnes, R., Quinn, T. R., et al. 2018, *Astron. J.*, 155, 60, doi: 10.3847/1538-3881/aaa301

Delrez, L., Murray, C. A., Pozuelos, F. J., et al. 2022, arXiv e-prints, arXiv:2209.02831. https://arxiv.org/abs/2209.02831

Dittmann, J. A., Irwin, J. M., Charbonneau, D., et al. 2017, *Nature*, 544, 333, doi: 10.1038/nature22055

do Amaral, L. N. R., Barnes, R., Segura, A., & Luger, R. 2022, *Astrophys. J.*, 928, 12, doi: 10.3847/1538-4357/ac53af

Dobrovolskis, A. R. 2009, *Icarus*, 204, 1, doi: 10.1016/j.icarus.2009.06.007

Dole, S. H. 1964, Habitable planets for man (Rand Corp.)

Dong, C., Jin, M., Lingam, M., et al. 2018, Proceedings of the National Academy of Science, 115, 260, doi: 10.1073/pnas.1708010115

Driscoll, P., & Bercovici, D. 2013, *Icarus*, 226, 1447, doi: 10.1016/j.icarus.2013.07.025

—. 2014, Physics of the Earth and Planetary Interiors, 236, 36, doi: 10.1016/j.pepi.2014.08.004

Driscoll, P. E., & Barnes, R. 2015, Astrobiology, 15, 739, doi: 10.1089/ast.2015.1325

Efroimsky, M., & Makarov, V. V. 2013, *Astrophys. J.*, 764, 26, doi: 10.1088/0004-637X/764/1/26

Elkins-Tanton, L. 2008, Earth and Planetary Science Letters, 271, 181

Ellis, K. M., & Murray, C. D. 2000, *Icarus*, 147, 129, doi: 10.1006/icar.2000.6399

Erkaev, N. V., Kulikov, Y. N., Lammer, H., et al. 2007, A&A, 472, 329, doi: 10.1051/0004-6361:20066929

Ferraz-Mello, S., Rodríguez, A., & Hussmann, H. 2008, Celestial Mechanics and Dynamical Astronomy, 101, 171. https://arxiv.org/abs/0712.1156

Garraffo, C., Drake, J. J., Dotter, A., et al. 2018, *Astrophys. J.*, 862, 90, doi: 10.3847/1538-4357/aace5d

Gillon, M., Triaud, A. H. M. J., Demory, B.-O., et al. 2017, *Nature*, 542, 456, doi: 10.1038/nature21360

Goldberg, M., & Batygin, K. 2022, arXiv e-prints, arXiv:2211.16725, doi: 10.48550/arXiv.2211.16725
Goldreich, P., & Soter, S. 1966, Icarus, 5, 375
Greenberg, R. 2009, Astrophys. J., 698, L42
Hayashi, C. 1961, PASJ, 13, 450
Heller, R., Leconte, J., & Barnes, R. 2011, Astro. & Astrophys., 528, A27+. https://arxiv.org/abs/1101.2156
Henning, W. G., O'Connell, R. J., & Sasselov, D. D. 2009, Astrophys. J., 707, 1000. https://arxiv.org/abs/0912.1907
Holman, M. J., & Murray, N. W. 2005, Science, 307, 1288, doi: 10.1126/science.1107822
Hunten, D. M., Pepin, R. O., & Walker, J. C. G. 1987, Icarus, 69, 532, doi: 10.1016/0019-1035(87)90022-4
Jackson, B., Barnes, R., & Greenberg, R. 2008a, *Mon. Not. R. Astron. Soc.*, 391, 237, doi: 10.1111/j.1365-2966.2008.13868.x
Jackson, B., Greenberg, R., & Barnes, R. 2008b, Astrophys. J., 681, 1631. https://arxiv.org/abs/0803.0026
Johnstone, C. P., Bartel, M., & Güdel, M. 2021, *Astron. & Astrophys.*, 649, A96, doi: 10.1051/0004-6361/202038407
Kasting, J. F., Whitmire, D. P., & Reynolds, R. T. 1993, *Icarus*, 101, 108, doi: 10.1006/icar.1993.1010
Kopparapu, R. K., Ramirez, R., Kasting, J. F., et al. 2013, *Astrophys. J.*, 765, 131, doi: 10.1088/0004-637X/765/2/131
Krissansen-Totton, J., & Fortney, J. J. 2022, *Astrophys. J.*, 933, 115, doi: 10.3847/1538-4357/ac69cb
Lambrechts, M., Morbidelli, A., Jacobson, S. A., et al. 2019, *Astron. & Astrophys.*, 627, A83, doi: 10.1051/0004-6361/201834229
Leconte, J., Chabrier, G., Baraffe, I., & Levrard, B. 2010, Astro. & Astrophys., 516, A64+. https://arxiv.org/abs/1004.0463
Luger, R., & Barnes, R. 2015, Astrobiology, 15, 119, doi: 10.1089/ast.2014.1231
Luger, R., Barnes, R., Lopez, E., et al. 2015, Astrobiology, 15, 57, doi: 10.1089/ast.2014.1215
Magaudda, E., Stelzer, B., Covey, K. R., et al. 2020, *Astron. & Astrophys.*, 638, A20, doi: 10.1051/0004-6361/201937408
Mardling, R. A., & Lin, D. N. C. 2002, Astrophys. J., 573, 829
Meadows, V. S., & Barnes, R. K. 2018, Factors Affecting Exoplanet Habitability (Springer), 57, doi: 10.1007/978-3-319-55333-7_57
Morrell, S., & Naylor, T. 2019, *Mon. Not. R. Astron. Soc.*, 489, 2615, doi: 10.1093/mnras/stz2242
Murray, C. D., & Dermott, S. F. 1999, Solar system dynamics (Cambridge University Press)
Murray-Clay, R. A., Chiang, E. I., & Murray, N. 2009, *Astrophys. J.*, 693, 23, doi: 10.1088/0004-637X/693/1/23
Owen, J. E., & Wu, Y. 2017, *Astrophys. J.*, 847, 29, doi: 10.3847/1538-4357/aa890a
Peacock, S., Barman, T., Shkolnik, E. L., et al. 2020, *Astrophys. J.*, 895, 5, doi: 10.3847/1538-4357/ab893a
Peale, S. J., Cassen, P., & Reynolds, R. T. 1979, Science, 203, 892, doi: 10.1126/science.203.4383.892
Pierrehumbert, R., & Gaidos, E. 2011, *Astrophys. J. Lett.*, 734, L13, doi: 10.1088/2041-8205/734/1/L13
Raymond, S. N., Barnes, R., Armitage, P. J., & Gorelick, N. 2008, *Astrophys. J. Lett.*, 687, L107, doi: 10.1086/593301
Raymond, S. N., Scalo, J., & Meadows, V. S. 2007, *Astrophys. J.*, 669, 606, doi: 10.1086/521587
Ribas, I., Guinan, E. F., Güdel, M., & Audard, M. 2005, Astrophys. J., 622, 680, doi: 10.1086/427977
Richey-Yowell, T., Shkolnik, E. L., Loyd, R. O. P., et al. 2022, *Astrophys. J.*, 929, 169, doi: 10.3847/1538-4357/ac5f48
Schaefer, L., Wordsworth, R. D., Berta-Thompson, Z., & Sasselov, D. 2016, *Astrophys. J.*, 829, 63, doi: 10.3847/0004-637X/829/2/63
Schlecker, M., Apai, D., Lichtenberg, T., et al. 2024, The Planetary Science Journal, 5, 3, doi: 10.3847/PSJ/acf57f
Stevenson, D. J. 1987, Annual Review of Earth and Planetary Sciences, 15, 271, doi: 10.1146/annurev.ea.15.050187.001415
Touma, J., & Wisdom, J. 1993, Science, 259, 1294, doi: 10.1126/science.259.5099.1294
Turbet, M., Ehrenreich, D., Lovis, C., Bolmont, E., & Fauchez, T. 2019, Astronomy & Astrophysics, 628, A12, doi: 10.1051/0004-6361/201935585

Veeder, G. J., Matson, D. L., Johnson, T. V., Blaney, D. L., & Goguen, J. D. 1994, *J. Geophys. Res.*, 99, 17095, doi: 10.1029/94JE00637

Watson, A. J., Donahue, T. M., & Walker, J. C. G. 1981, Icarus, 48, 150, doi: 10.1016/0019-1035(81)90101-9

Wu, Y., & Goldreich, P. 2002, *Astrophys. J.*, 564, 1024, doi: 10.1086/324193